

# PCCP

Accepted Manuscript



This is an *Accepted Manuscript*, which has been through the Royal Society of Chemistry peer review process and has been accepted for publication.

*Accepted Manuscripts* are published online shortly after acceptance, before technical editing, formatting and proof reading. Using this free service, authors can make their results available to the community, in citable form, before we publish the edited article. We will replace this *Accepted Manuscript* with the edited and formatted *Advance Article* as soon as it is available.

You can find more information about *Accepted Manuscripts* in the [Information for Authors](#).

Please note that technical editing may introduce minor changes to the text and/or graphics, which may alter content. The journal's standard [Terms & Conditions](#) and the [Ethical guidelines](#) still apply. In no event shall the Royal Society of Chemistry be held responsible for any errors or omissions in this *Accepted Manuscript* or any consequences arising from the use of any information it contains.

## *In situ* magnetic and electronic investigation of the early stage oxidation of Fe nanoparticles using x-ray photo-emission electron microscopy

Cite this: DOI: 10.1039/x0xx00000x

C. A. F. Vaz,<sup>a</sup> A. Balan,<sup>a</sup> F. Nolting<sup>a</sup> and A. Kleibert<sup>a</sup>,

Received 00th January 2012,  
Accepted 00th January 2012

DOI: 10.1039/x0xx00000x

[www.rsc.org/](http://www.rsc.org/)

We present an *in situ* experimental investigation of the magnetic and electronic properties of individual iron nanoparticles with sizes ranging from 8 to 22 nm as a function of oxygen exposure (0-80 L), using x-ray photoemission electron microscopy. The x-ray absorption spectroscopy results show that, irrespective of size and magnetic state, the early stages of the Fe nanoparticle oxidation occur through the initial formation of a non-magnetic FeO-like layer, followed by a progressive transformation of the latter to Fe<sub>3</sub>O<sub>4</sub>. At 80 L, the metallic iron core and the outer Fe<sub>3</sub>O<sub>4</sub> shell are separated by a thin FeO layer. Our data suggest that the outer Fe<sub>3</sub>O<sub>4</sub> layer has either a magnetic order that significantly differs from the respective bulk or that the FeO-like layer is responsible for a magnetic decoupling between the Fe<sub>3</sub>O<sub>4</sub> shell and the iron core. Moreover, we find that the recently observed blocked magnetic state in the pure metallic iron nanoparticles persists upon oxygen exposure, demonstrating that the enhanced magnetic energy barriers do not originate from the free surface of the nanoparticles.

### Introduction

The last few years have seen a rapidly growing interest in nanoparticles and in the physical mechanisms underlying their behaviour due to their great technological importance in fields ranging from catalysis to magnetic data storage.<sup>1-7</sup> Low dimensionality systems exhibit a variety of unusual magnetic phenomena when compared to their bulk counterparts, such as enhanced magnetic moments or magnetic anisotropies, mostly associated with surface/interface finite-size effects.<sup>8-13</sup> For example, recent results showed the presence of large magnetic anisotropies in Fe nanoparticles responsible for stabilising ferromagnetism at room temperature, whereas a superparamagnetic behaviour would be expected from the bulk magnetocrystalline anisotropy of Fe.<sup>14</sup> A good control over the magnetic anisotropy in such systems could be of potential interest for applied research, for example for applications in high density storage media and for magnetic tags in biological assays.<sup>15, 16</sup>

Also of topical interest is the study of iron/iron-oxide core-shell particles, which, in addition to their interesting magnetic properties, have shown to be useful for applications in medicine as potential drug delivery and as contrast agents for magnetic resonance imaging.<sup>17-19</sup> The iron-oxide shell is mainly used to passivate the chemically reactive iron core, but magnetic interactions between the shell and the ferromagnetic core have been observed at lower temperatures.<sup>7, 20, 21</sup> The latter is important when attempting to employ exchange coupling phenomena in applications.<sup>21</sup> Previous studies on the oxidation

of pure iron particles revealed that oxidation either by exposure to ambient air or to pure oxygen leads to the formation of an oxide shell with a thickness 2-3 nm, with the oxide shell adjacent to the ferromagnetic metal core dominated by Fe<sub>3</sub>O<sub>4</sub>, and with an outer shell mainly composed of  $\gamma$ -Fe<sub>2</sub>O<sub>3</sub>.<sup>17, 20, 22-25</sup> Recent experiments revealed a defective structure of the oxide shell, but the magnetic properties of the latter were not addressed.<sup>25</sup> Further, most of the previous studies focus on the properties after the formation of the oxide shell, and thus a direct study of the chemical composition of iron nanoparticles during the growth of the oxide shell and a correlation with its magnetic properties is still lacking. Finally, the recent discovery of metastable magnetic properties in pure iron nanoparticles may suggest different electronic properties for iron particles in structurally excited or relaxed states, with correspondingly distinct chemical reaction paths.<sup>14</sup>

In this paper, we report on the evolution of the magnetic and electronic properties of individual Fe nanoparticles with sizes in the range from 8-22 nm during the early stages of oxidation, by measuring *in situ* x-ray absorption spectra using photoemission electron microscopy.<sup>26-29</sup> Our results indicate that, in the range from 0-80 L (1 L = 10<sup>-6</sup> torr s)<sup>30</sup> oxygen dosage, the oxidation process occurs in three distinct steps, irrespective of the particle size and the initial magnetic state: (i) formation of an FeO-like shell surrounding the metallic core; (ii) conversion of the outer part of the FeO to Fe<sub>3</sub>O<sub>4</sub>; and (iii) consumption of the FeO to a dominant Fe<sub>3</sub>O<sub>4</sub> oxide shell surrounding a metallic Fe core. The Fe<sub>3</sub>O<sub>4</sub> shell appears non-magnetic, which is either due to a magnetic decoupling from the ferromagnetic Fe core by the

non-magnetic FeO layer or due to a lack of magnetic order in the Fe<sub>3</sub>O<sub>4</sub> layer, possibly as a consequence of the defective structure of the oxide shell.<sup>25</sup> Further, we find that particles that are ferromagnetic immediately after deposition remain magnetically blocked upon oxygen exposure, indicating that the large magnetic anisotropies responsible for the stabilisation of the ferromagnetic state does not originate from the Fe/vacuum interface.<sup>14</sup>

Critical to these investigations is the possibility of carrying out experiments in conditions that preserve the pristine condition of the nanoparticles, before and after oxygen exposure. This requires the deposition of the particles under ultrahigh vacuum conditions and the capability of carrying out the measurements *in situ* immediately after deposition. Here, we use an arc cluster ion source (ACIS) connected in ultrahigh vacuum to a photoemission electron microscope (PEEM) to investigate the electronic and magnetic properties of individual Fe nanoparticles.<sup>31</sup> Previous transmission electron microscopy investigations of ACIS-generated nanoparticles reveal that most particles are single crystalline with the bcc lattice known from the bulk and have a compact shape close to the thermal equilibrium shape predicted by a Wulff construction as illustrated in Figure 1a, making them valuable model systems for the study of magnetism in nanoparticles.<sup>31, 32</sup> Further, the present approach allows us to distinguish the intrinsic properties of well-separated and non-interacting nanoparticles from phenomena which result from the complex magnetic interactions found in dense particle ensembles.<sup>29, 33</sup>

## Experimental

The iron nanoparticles studied here are generated in the gas phase using an ACIS system and are deposited *in situ* onto passivated Si(001) wafers, which are held in a surface preparation chamber with a base pressure of  $5 \times 10^{-10}$  mbar. Prior to the particle deposition the substrates are thermally annealed for about 20 minutes at 200°C. This procedure removes adsorbates from the substrates, present from ambient air exposure before the transfer into the vacuum system, but keeps the native, amorphous SiO<sub>x</sub> surface layer intact. After cooling down to room temperature particles with sizes  $D$  in the range of 8–22 nm are deposited. The deposition takes place under so-called soft landing conditions, i.e., fragmentation or damage of the particles or the substrates is avoided.<sup>34</sup> The particle density on the surface is limited to a few ( $< 10$ ) particles per  $\mu\text{m}^2$  to enable single particle detection with x-ray PEEM, which has a spatial resolution of about 50–100 nm, and to avoid interactions between the particles.<sup>35</sup> The stochastic nature of the deposition process leads to a random spatial distribution and a random crystallographic orientation of the nanoparticles with respect to the substrate.<sup>36</sup> Upon deposition the samples are transferred *in situ* to the PEEM instrument at the Surface/Interface: Microscopy (SIM) beamline of the Swiss Light Source, Paul Scherrer Institut, Switzerland.<sup>37, 38</sup> The base pressure in the microscope was  $5 \times 10^{-10}$  mbar for the present experiments. Oxidation of the nanoparticles was carried out by leaking molecular oxygen to the system at a partial pressure of  $1 \times 10^{-8}$  mbar from 0 L to 30 L in discrete steps as follows: 0.5 L ( $t_s = 67$  s), 1.0 L ( $t_s = 133$  s), 1.0 L ( $t_s = 133$  s), 2.5 L ( $t_s = 333$  s), 5.0 L ( $t_s = 665$  s), 10.0 L ( $t_s = 1330$  s), and 10.0 L ( $t_s = 1330$  s). Exposure between 30 L and 80 L was performed at a partial pressure of  $2 \times 10^{-8}$  mbar in the following steps: 10 L ( $t_s = 665$  s), 20 L ( $t_s = 1330$  s), and 20 L ( $t_s = 1330$  s). Each step was followed by magnetic characterisation employing the x-ray magnetic circular dichroism (XMCD) effect as described below. X-ray absorption spectra (XAS) of the particles were recorded after 0 L, 5 L, 30 L, and 80 L. During oxygen dosage,

the sample was protected from x-ray exposure to avoid possible x-ray induced chemical reactions. Also, before performing x-ray PEEM measurements, the system was allowed to recover to the base pressure in order to exclude ongoing oxidation during measurements. All measurements were carried out in the same area of the sample, on the same nanoparticles. While X-ray PEEM yields information about the magnetic and electronic properties of the well-separated individual particles, its limited spatial resolution prevents a detailed morphological characterization. Thus, after the PEEM experiments, the sample was further investigated *ex situ* by scanning electron microscopy (SEM), cf. Figure 1b, and atomic force microscopy (AFM) to accurately determine the shape and size of the individual nanoparticles investigated with PEEM, cf. the Electronic Supplementary Information. For identification of the very same particles in the different microscopes, the substrates have lithographic Cr/Au markers. All experiments and the oxygen dosage were carried out at room temperature.

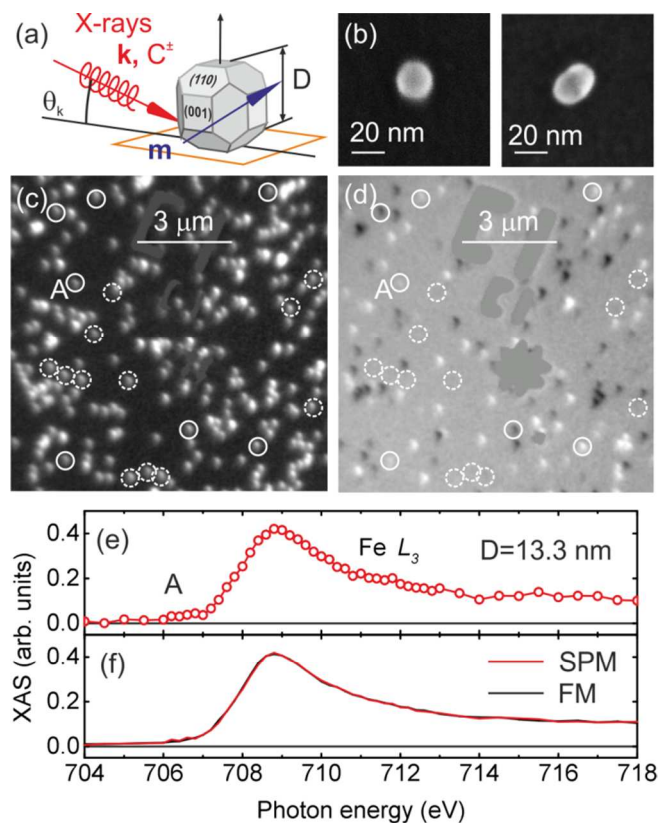


Fig. 1 (a) Experimental geometry for the x-ray PEEM experiments and schematic of an iron nanoparticle with a shape as predicted at thermal equilibrium. (b) *Ex situ* high resolution scanning electron microscopy images recorded after the x-ray PEEM experiments. The particle on the left hand side shows a highly symmetric shape close to the scheme in (a). The particle on the right hand side displays an elongated shape and is excluded from further analysis in the present work. (c) An x-ray PEEM elemental contrast map showing the distribution of nanoparticles on the sample. (d) Magnetic contrast map of the same area. A fraction of the particles shows magnetic contrast at room temperature (solid circles). The other particles show no magnetic contrast (dashed circles). (e) Isotropic x-ray absorption spectra of the particle labelled A in (c) and (d), 13.3 nm in diameter. (f) Averaged x-ray absorption spectra of superparamagnetic (SPM) and ferromagnetic (FM) nanoparticles.

X-ray PEEM elemental contrast maps (cf. Figure 1c), are obtained by pixelwise division of two images successively recorded with the photon energy set to the Fe  $L_3$  absorption edge (709 eV) and at a pre-edge energy (703 eV). Magnetic

properties are probed by recording images with circularly polarized x-rays and the photon energy tuned to the Fe  $L_3$  edge. The XMCD effect leads then to a magnetization dependent intensity of the particles according to  $I(C^\pm) = I_0 \pm \gamma \mathbf{k} \cdot \mathbf{m}$ , where  $I_0$  is the isotropic (non-magnetic) intensity,  $\mathbf{k}$  is the x-ray propagation vector with an angle of incidence  $\theta_k = 16^\circ$ ,  $\mathbf{m}$  is the magnetization vector of the particle,  $\gamma$  is a material and photon energy dependent constant, and  $C^\pm$  denote circular right- and left-handed photon polarization (cf. Figure 1a). Magnetic contrast maps are then obtained by pixelwise division of both images. The contrast is therefore proportional to  $\mathbf{k} \cdot \mathbf{m}$ , which leads to “white” and “black” spots for particles with  $\mathbf{m}$  (fully or partially) parallel or antiparallel to  $\mathbf{k}$ , respectively, as observed in Figure 1d. Typical integration times for each magnetic image are  $\sim 20$  s. To obtain high quality magnetic contrast maps, as shown in Figure 1d, twenty of these images are averaged. Isotropic XAS are obtained by recording a sequence of x-ray PEEM images at various photon energies across the Fe  $L_3$  edge using linearly, s-polarised light and analysing  $I_0$  as a function of photon energy.<sup>27, 39</sup>

## Results and Discussion

To univocally determine the presence and position of the Fe nanoparticles, we first measure an elemental contrast map of the sample as-grown, a representative result of which is given in Figure 1c, showing the iron nanoparticles appearing as bright spots. We find that the particles are almost randomly distributed with a density of about 5 particles per  $\mu\text{m}^2$ , when averaging over a sufficiently large area of the sample. The random distribution of the particles on the surface reflects the stochastic nature of the deposition process and the limited mobility of the particles on the surface.<sup>35</sup> Ideally, each bright spot should correspond to an individual iron nanoparticle, with a shape similar to the scheme in Figure 1a. However, subsequent SEM measurements on the same area of the sample reveal that several particles have a distorted shape, for example, elongated (Figure 1b, right). To avoid complications associated with shape effects, only well-shaped and well separated particles (including those circled in the left-hand image in Figure 1b) are selected for analysis here.

The magnetic characterisation of the metallic Fe nanoparticles shows that about half of the particles exhibit magnetic contrast at room temperature (particles within solid circles in Figures 1c and d. The other half shows no magnetic contrast (dashed circles). These results are in agreement with recent results, where it was further shown that this observation is due the presence of magnetically blocked and superparamagnetic particles, respectively, independently of particle size.<sup>14</sup> While the first show a wide range of magnetic contrast values due to their random orientation on the substrate upon deposition, the latter show no magnetic contrast due to thermally activated switching of their magnetization at a rate much faster than the time resolution of the experiment.<sup>14</sup> The XAS at the Fe  $L_3$  edge of a single particle before dosing oxygen is shown in Figure 1e, which is representative of the data quality that can be attained in PEEM. We find that all single particle spectra are similar and resemble that of pure, metallic iron.<sup>40</sup> To check for differences in the electronic structure between superparamagnetic and ferromagnetic nanoparticles, we averaged the spectra of 18 superparamagnetic (red line) and 12 ferromagnetic particles (black line), as depicted in Figure 1f. The comparison shows that both types of particles are electronically equivalent in the surface near shell, of about 2 to 3 nm probed by x-ray PEEM.

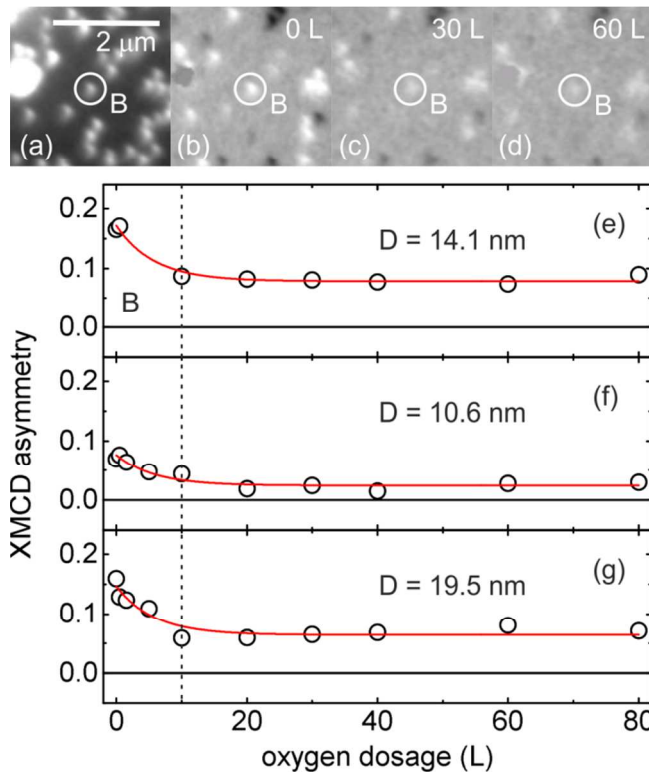


Fig. 2 (a) X-ray PEEM elemental contrast map recorded with the photon energy set to the  $L_3$  edge of metallic iron ( $\text{Fe}^0 L_3$ ). (b) – (d) Magnetic contrast maps of the same area as in (a) recorded upon dosing the denoted amount of oxygen. The ferromagnetic particle B is highlighted with a solid circle in all images. (e) – (g) XMCD asymmetry of three ferromagnetic particles with different sizes (as labelled), as a function of oxygen dosage. The red lines are guides to the eye. (e) shows data for particle B.

The effect of dosing molecular oxygen on the magnetic properties is directly seen as a gradual decrease in the magnetic contrast of the ferromagnetic particles, as shown in Figure 2b-d. In a few cases, a sudden total loss of magnetic contrast is also observed, which we assign to the previously reported spontaneous relaxation of the metastable ferromagnetic to the superparamagnetic ground state.<sup>14</sup> A quantitative measure of the magnetic contrast is obtained by calculating the normalized XMCD asymmetry, given by  $[I(C^+) - I(C^-)]/[I(C^+) + I(C^-)]$ , for individual ferromagnetic nanoparticles.<sup>14</sup> The analysis reveals that the largest loss of magnetic contrast occurs already after the first 10 L of oxygen as demonstrated for three particles in Figure 2e-g. Further oxygen dosage has only little or no effect on the remaining XMCD asymmetry, which typically saturates to 50% of the unexposed value for exposures above 20 L. Figure 2e-g also shows that the saturation effect is independent of the particle size. Again, it is worth emphasizing that all ferromagnetic particles, with the exception of those that spontaneously transition to the superparamagnetic state, still demonstrate a stable magnetization after dosing 80 L  $\text{O}_2$ , i.e., irrespective of the formation of an oxide shell. This result suggests that the origin of the large magnetic anisotropy exhibited by these particles resides either in the core of the nanoparticle or else at the interface with the substrate, which we may assume remains unaffected by the oxygen exposure down to the doses and time scales considered in this study.

To determine the evolution of the oxide shell formation, we turn to the results of isotropic XAS at the Fe  $L_3$  edge taken after successive dose exposures. In all cases the individual particle spectra are similar and no differences between the ferromagnetic and the superparamagnetic particles or any size dependent signatures are

found. Hence, we have averaged the spectra of the 18 SPM nanoparticles in order to improve the signal to noise ratio. The data thus processed are shown in Figure 3 for different O<sub>2</sub> dosages. It is observed that oxygen dosage leads to the emergence of a strong resonance at about 1.4 eV above the energy of the metallic Fe L<sub>3</sub> peak. We note that the L<sub>3</sub> edge maximum in metallic iron (Fe<sup>0</sup>) coincides with the L<sub>3</sub> edge peak of Fe<sup>2+</sup> ion in FeO, while the L<sub>3</sub> edge maxima of Fe<sub>3</sub>O<sub>4</sub> and γ-Fe<sub>2</sub>O<sub>3</sub> corresponding to the Fe<sup>3+</sup> ion contribution overlap, as indicated in Figure 3.<sup>40, 41</sup> Thus, a direct determination of the oxide shell composition from the XAS is challenging. However, more insight is obtained when correlating the XAS with the magnetic contrast results shown in Figure 2. Most notably, we observe that the magnetic contrast does not change after dosing about 10 L of oxygen, while the x-ray absorption spectra show a continuous increase of Fe<sub>3</sub>O<sub>4</sub> or γ-Fe<sub>2</sub>O<sub>3</sub> up to the maximum dosage of 80 L studied here. Since both these oxides are ferrimagnetic at room temperature, the latter observation suggests either the absence of magnetic interactions between the oxide shell and the magnetic iron core and/or that the magnetic properties of the oxide shell deviate strongly from the bulk.

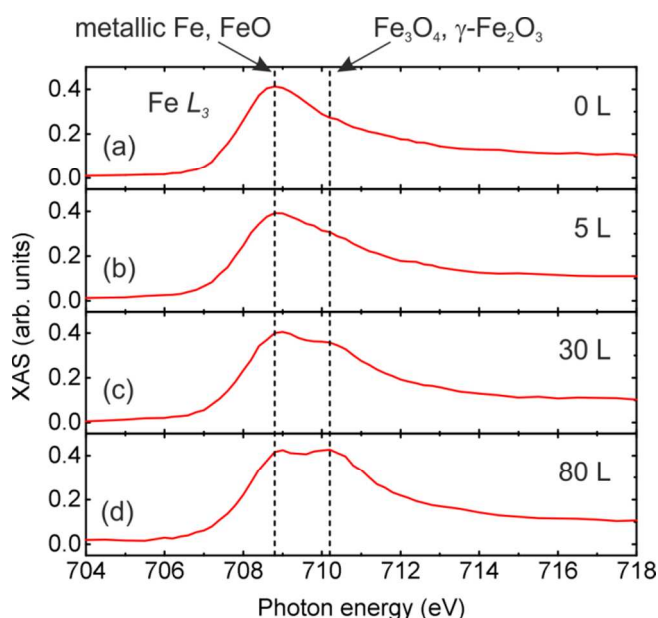


Fig. 3 (a) – (d) X-ray absorption spectra in the vicinity of the Fe L<sub>3</sub> edge as a function of oxygen dosage (red lines). The photon energies corresponding to the L<sub>3</sub> edge maxima of metallic Fe, FeO, Fe<sub>3</sub>O<sub>4</sub>, and γ-Fe<sub>2</sub>O<sub>3</sub> are denoted by the dashed lines.

To gain more quantitative insight into the oxide shell formation, we simulate the x-ray absorption spectra by considering that the intensity in the x-ray PEEM images is proportional to the number of electrons which are released at various depths in the sample upon absorption of the x-rays.<sup>40</sup> In a core-shell system it is essential to consider that (i) the local intensity of the incident x-rays in the particle does not simply decay exponentially with the penetration depth, but is further modulated by the varying absorption cross sections of the different layers at a given photon energy and (ii) that the emitted electrons will also experience a material dependent attenuation when leaving the sample.<sup>40</sup> In the simulation, we consider a progression of the oxidation starting from the metallic core as Fe<sup>0</sup>:FeO:Fe<sub>3</sub>O<sub>4</sub>, which we model by considering a metallic Fe substrate covered by the two oxide layers with variable thicknesses.<sup>42</sup> For simplicity, we neglect γ-Fe<sub>2</sub>O<sub>3</sub>, which has a spectral signature very similar to Fe<sub>3</sub>O<sub>4</sub> (Refs. 33,40) and is difficult

to distinguish from the latter. Moreover, its presence is only expected at higher oxygen exposures (which is also the case for α-Fe<sub>2</sub>O<sub>3</sub>).<sup>23</sup> The x-ray cross sections for the isotropic spectra and the magnetic contrast for Fe, FeO and Fe<sub>3</sub>O<sub>4</sub> are taken from Refs. 40 and 41. The effective electron escape depth is 17 Å for Fe, 30 Å for FeO and 50 Å for Fe<sub>3</sub>O<sub>4</sub>.<sup>40</sup> Finally, perpendicular incidence of the x-rays on the simulated layer stack is assumed, cf. the Electronic Supplementary Information. The magnetization **m** of the ferro- or ferrimagnetic layers is set parallel or antiparallel to **k**. We may note that this semi-infinite approximation is an adequate approximation to a supported nanoparticle since the escape depth of the detected electrons is limited to about 3-5 nm and in PEEM mostly the electrons emitted normal to the surface are captured.<sup>32, 43</sup> Hence, for the particle size that we investigate here, PEEM probes only the topmost part of the outermost layers and part of the bulk of the nanoparticle. The model is further justified by the experimental observation that the evolution of the x-ray absorption spectra does not depend on the particle size, as stated above.

In Figure 4a-d we show the simulated isotropic XAS together with the experimental data. The thickness for the oxide layers that provide the best agreement with the experimental spectra and magnetic contrast values at the Fe L<sub>3</sub> edge are indicated in the panels and plotted together with the total oxide shell thickness as a function of O<sub>2</sub> exposure in Figure 5. The simulated magnetic contrast at the Fe L<sub>3</sub> edge, which includes the effect of the altered XAS line shape (cf. the Electronic Supplementary Information), is shown in Figure 4e together with the experimental data at each step of the experiment for particle B of Figure 2e, which is representative for the ferromagnetic particles. The simulated contrast has been scaled to the experimental value for this particle at 0 L, since it depends on the relative orientation of its magnetization **m** to the photon propagation vector **k**, which was not explicitly determined in the present experiments. The variation of the magnetic contrast with oxygen dosage provides a strong constraint in these simulations and significant deviations from either the experimental XAS or the experimental magnetic contrast or both are already observed when varying the thickness parameters by more than 2 Å in the simulations.

From the simulations we draw the following conclusions: (i) we can exclude a ferromagnetic or antiferromagnetic coupling of a Fe<sub>3</sub>O<sub>4</sub> shell with bulk-like magnetic order to the metallic Fe core in our experiments. This is a consequence of the fact that ferromagnetic Fe<sub>3</sub>O<sub>4</sub> has a sizeable magnetic contrast at the Fe<sup>0</sup> L<sub>3</sub> peak energy, and thus a ferromagnetic coupling of Fe<sub>3</sub>O<sub>4</sub> to the Fe<sup>0</sup> core would result in an increase of the magnetic contrast amplitude proportional to the amount of Fe<sub>3</sub>O<sub>4</sub> present in the nanoparticle, particularly above 20 L. In case of an antiferromagnetic coupling, the magnetic contrast of the Fe<sub>3</sub>O<sub>4</sub> would have the opposite sign relative to the Fe<sup>0</sup> core, and thus would cancel part of the total contrast. As a consequence, the magnetic contrast would decrease with increasing Fe<sub>3</sub>O<sub>4</sub> content, which is not observed experimentally either. (ii) A non-magnetic (or superparamagnetic) Fe<sub>3</sub>O<sub>4</sub> shell alone cannot explain the drop of magnetic contrast found experimentally, since the absorption cross section of Fe<sub>3</sub>O<sub>4</sub> is relatively weak at the Fe<sup>0</sup> L<sub>3</sub> peak energy (709 eV). Thus, a much larger XAS contribution of Fe<sub>3</sub>O<sub>4</sub> would be expected when compared to our experimental data. For instance, a thickness of 23 Å would be required to explain the reduced magnetic contrast observed at 30 L, which would lead to an Fe<sub>3</sub>O<sub>4</sub> L<sub>3</sub> peak much higher in amplitude than that observed experimentally, even at 80 L. (iii) The previous points suggest that the initial loss in magnetic contrast must result from the formation of a non-magnetic FeO layer with its relatively high absorption cross section at the Fe<sup>0</sup> L<sub>3</sub> peak energy. Indeed, only when considering a FeO layer in the

simulations the loss of magnetic contrast and the XAS can be simultaneously reproduced as shown in Figure 4. Further details of the simulations are presented in the Electronic Supplementary Information.

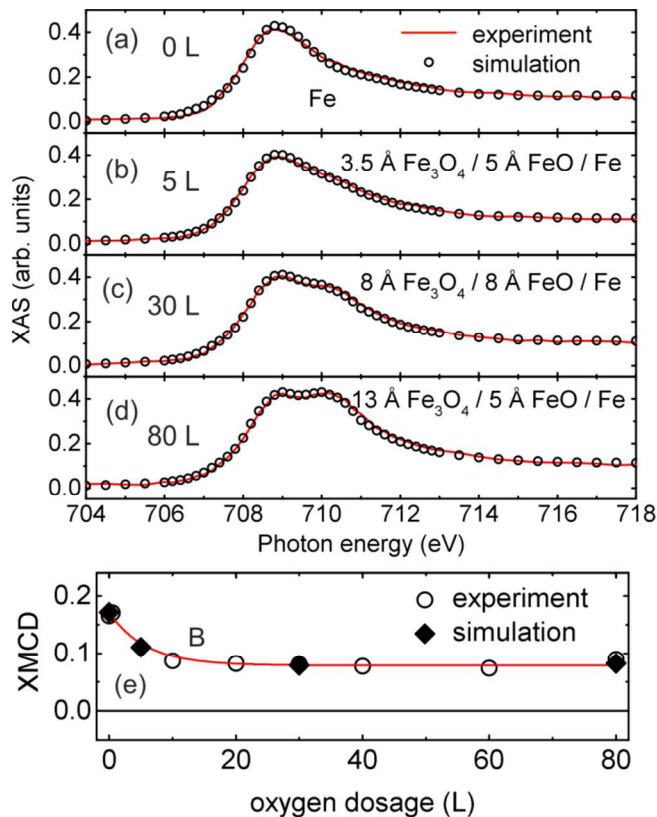


Fig. 4 (a-d) Simulated x-ray absorption spectra (XAS) at the Fe  $L_3$  edge as a function of oxygen dosage (circles) compared to the experimental data (red lines). The corresponding layer thicknesses used in the simulations are as denoted. (e) Magnetic contrast at the Fe $^0$   $L_3$  edge obtained from simulations (diamonds) and experiment for particle B in Figure 2(e) (circles). Line is a guide to the eye.

The thickness of the oxide layers and of the resulting total oxide shell as used in the simulations is displayed as a function of the oxygen dosage in Figure 5. It is seen that a sizeable oxide shell is already formed after 5 L molecular oxygen, which is due to the high oxygen affinity of iron. Upon further exposure, the total oxide shell approaches 18 Å at 80 L, which is close to the value reported for the saturated oxide shell formed upon exposure of pure iron nanoparticles to ambient air, typically 20-30 Å. Our simulations indicate that the composition of the oxide shell changes with increasing O<sub>2</sub> exposure. Hence, our results allow us to obtain the following picture for the early stages of oxidation of magnetic Fe nanoparticles: first, a non-magnetic FeO-like layer is formed at the iron surface, which leads to a rapid loss of magnetic volume (Fe $^0$ ) and magnetic contrast in x-ray PEEM (0-20 L). Further oxidation leads to the formation of a layer of the more stable Fe<sub>3</sub>O<sub>4</sub> at the vacuum interface, but with the intermediate non-magnetic FeO layer still present (20-80 L). This non-magnetic FeO layer is expected to have an important impact on the magnetic properties of the nanoparticles: first, provided that the thin Fe<sub>3</sub>O<sub>4</sub> layer would possess a bulk-like ferrimagnetic order, the FeO could give a natural explanation for the observed magnetic decoupling of the Fe<sub>3</sub>O<sub>4</sub> shell from the metallic Fe core. Second, given that bulk FeO is antiferromagnetic with a Néel temperature of 198 K, the presence of this oxide layer could further provide the key to understanding the

observation of exchange bias effects in oxidized iron nanostructures at lower temperatures.<sup>21, 44</sup> One example of the impact of the interfacial oxidation state on the exchange bias effect is provided by the Ni/Co<sub>3</sub>O<sub>4</sub>(110) system, where the observation of a blocking temperature that is much higher than the Néel temperature of bulk Co<sub>3</sub>O<sub>4</sub> (40 K) is attributed to the formation of an interfacial CoO layer.<sup>45</sup>

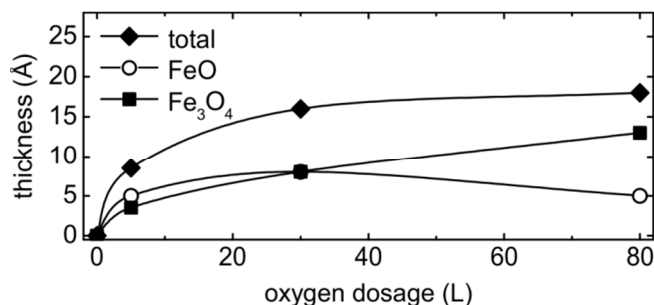


Fig. 5 Evolution of the thickness and composition of the oxide shell as a function of oxygen dosage as obtained from the simulations. Black lines are guides to the eye.

We note that the presence of bulk-like FeO in oxidized iron nanoparticles has been excluded from Mössbauer spectroscopy, x-ray and electron diffraction, or high resolution transmission electron microscopy.<sup>17, 22, 25</sup> However, in contrast to these experiments, our work focuses on the initial stages of oxidation, where the amount of oxygen dosage is orders of magnitudes lower. Moreover, the direct local probing of the XAS on single nanoparticles might provide a different sensitivity compared to the techniques mentioned above. In fact, an intermediate, non-magnetic FeO-like layer has also been observed in the XAS of iron-iron oxide core-shell systems.<sup>33</sup> Recent electron energy loss spectroscopy investigations revealed a strongly enhanced amount of Fe<sup>2+</sup> in oxidized nanoparticles, which was interpreted as defective Fe<sub>3</sub>O<sub>4</sub>.<sup>25</sup> This observation is consistent with the presence of Fe<sup>2+</sup> in the intermediate FeO-like layer found here and the oxide layers studied in the present work could correspond to the defective Fe<sub>3</sub>O<sub>4</sub> layer with a thickness-dependent composition. Our data would further suggest that, at room temperature, this layer is either non-magnetic (disordered) or magnetically decoupled from the magnetic iron core due to the defects.

Moreover, the surface reaction with oxygen allows us to gain important insight into the origin of the anomalous high magnetic anisotropy of the ferromagnetically blocked iron nanoparticles.<sup>14</sup> Various contributions may establish the effective magnetic energy barriers of magnetic nanoparticles.<sup>4, 10, 46</sup> In particular, the particle surface can give rise to a significant surface anisotropy contribution.<sup>46, 47</sup> The present experiments address this issue directly, since we are capable of observing the magnetism of isolated and well-defined particles *in situ*, as a function of the oxidation process. As revealed by our data, oxygen leads to a chemical reaction which drastically alters properties of the surface layer, but the magnetic stability of the initially ferromagnetic particles is not affected (Figure 2). This clearly demonstrates that the free surface of the iron nanoparticles is not responsible for the anomalous magnetic anisotropy. In addition, the oxidation causes a sizeable loss of the ferromagnetic iron volume. For instance, we may consider a spherical, pure iron particle with an initial diameter of  $D_{Fe} = 9$  nm. Upon dosing 80 L oxygen an oxide shell of about 2 nm is formed (cf. Figure 5). Due to incorporation of oxygen ions into the oxide shell the total particle diameter will increase, while the remaining metallic core will have a reduced diameter. The resulting size and the diameter of the metallic core can be estimated when knowing the

atomic densities of the involved oxides. For simplicity, we may assume that the oxide shell consists solely of  $\text{Fe}_3\text{O}_4$  with bulk-like density. For the considered particle, this yields a total diameter of about 11 nm and a metallic core with a diameter of about  $D_{\text{Fe}}^* = 7$  nm after oxidation. Accordingly, the volume of ferromagnetic iron in this particle is reduced by a factor of two. This situation compares to the particle in Figure 2f, which remains ferromagnetic in the experiment. These data illustrate that even a significant loss of magnetic volume does not affect the magnetic stability of the initially blocked particles. This finding further supports that the origin for the large magnetic anisotropy barrier is indeed very local and resides deep in the particle volume, e.g. due to dislocations, as suggested previously,<sup>14</sup> point defects, or at the interface with the substrate, which is most likely not affected by the oxidation. In addition, these results demonstrate that chemical reaction with oxygen under the present conditions does not cause the relaxation of the metastable ferromagnetic state towards the superparamagnetic state by inducing a structural relaxation to bulk-like properties.<sup>14</sup>

## Conclusions

An *in situ* study of the oxidation of iron nanoparticles has been carried out using x-ray PEEM to follow the formation and evolution of the oxide shell in individual nanoparticles by means of spectro-microscopy. Both the size and shape of the particles has been determined from subsequent *ex situ* SEM and AFM measurements. We find that the oxide shell growth is not correlated with the particle size or initial magnetic state and that the oxidation process is very homogenous within the particle ensemble. We demonstrate that the oxidation starts through the formation of a non-magnetic FeO-like layer with a thickness of about 5 Å at the lowest oxygen exposures (0-20 L). With increasing oxygen dosage, the outer oxide shell is converted to  $\text{Fe}_3\text{O}_4$  and coexists with the intermediate oxide layer surrounding the metallic core. Our results suggest that the non-magnetic interlayer may lead to a magnetic decoupling between the metallic Fe core and the outer  $\text{Fe}_3\text{O}_4$  shell. Further, we find that the anomalous high magnetic anisotropy of the ferromagnetically blocked nanoparticles is not affected by altering the particle surface and the transformation of a significant volume of metallic iron into iron oxide, which may provide further evidence for a very localized origin of the unusual magnetic energy barriers. The data also demonstrate that, even when electronic and chemical surface properties of nanoparticles appear homogenous and size-independent in a mono-disperse ensemble, their magnetic behaviour can still show striking local variability.

## Acknowledgements

This work was supported by the Swiss Nanoscience Institute, University of Basel. Part of this work was performed at the Surface/Interface: Microscopy (SIM) beam line of the Swiss Light Source, Paul Scherrer Institut, Villigen, Switzerland. The use of LMN facilities (AFM, SEM) is duly acknowledged.

## Notes and references

<sup>a</sup> Swiss Light Source, Paul Scherrer Institut, 5232 Villigen PSI, Switzerland.

1. W. P. Halperin, *Reviews of Modern Physics*, 1986, **58**, 533-606.
2. L. N. Lewis, *Chem Rev*, 1993, **93**, 2693-2730.
3. A. P. Alivisatos, *Science*, 1996, **271**, 933-937.

4. X. Batlle and A. Labarta, *J Phys D Appl Phys*, 2002, **35**, R15-R42.
5. S. Sun, C. B. Murray, D. Weller, L. Folks and A. Moser, *Science*, 2000, **287**, 1989-1992.
6. V. F. Puentes, K. M. Krishnan and A. P. Alivisatos, *Science*, 2001, **291**, 2115-2117.
7. A. H. Lu, E. L. Salabas and F. Schuth, *Angewandte Chemie*, 2007, **46**, 1222-1244.
8. V. Skumryev, S. Stoyanov, Y. Zhang, G. Hadjipanayis, D. Givord and J. Nogues, *Nature*, 2003, **423**, 850-853.
9. S. Rusponi, T. Cren, N. Weiss, M. Epple, P. Bulushek, L. Claude and H. Brune, *Nature materials*, 2003, **2**, 546-551.
10. J. Bansmann, S. H. Baker, C. Binns, J. A. Blackman, J. P. Bucher, J. Dorantes-Davila, V. Dupuis, L. Favre, D. Kechrakos, A. Kleibert, K. H. Meiwes-Broer, G. M. Pastor, A. Perez, O. Toulemonde, K. N. Trohidou, J. Tuaille and Y. Xie, *Surface Science Reports*, 2005, **56**, 189-275.
11. C. Antoniak, M. E. Gruner, M. Spasova, A. V. Trunova, F. M. Romer, A. Warland, B. Krumme, K. Fauth, S. H. Sun, P. Entel, M. Farle and H. Wende, *Nature communications*, 2011, **2**.
12. A. Hillion, A. Cavallin, S. Vlaic, A. Tamion, F. Tournus, G. Khadra, J. Dreiser, C. Piamonteze, F. Nolting, S. Rusponi, K. Sato, T. J. Konno, O. Proux, V. Dupuis and H. Brune, *Physical Review Letters*, 2013, **110**.
13. C. A. F. Vaz, J. A. C. Bland and G. Lanhoff, *Reports on Progress in Physics*, 2008, **71**, 056501.
14. A. Balan, P. M. Derlet, A. F. Rodríguez, J. Bansmann, R. Yanes, U. Nowak, A. Kleibert and F. Nolting, *Physical Review Letters*, 2014, **112**.
15. B. D. Terris and T. Thomson, *J Phys D Appl Phys*, 2005, **38**, R199-R222.
16. D. L. Huber, *Small*, 2005, **1**, 482-501.
17. A. Pratt, L. Lari, O. Hovorka, A. Shah, C. Woffinden, S. P. Tear, C. Binns and R. Kroger, *Nature materials*, 2014, **13**, 26-30.
18. Y. Qiang, J. Antony, A. Sharma, J. Nutting, D. Sikes and D. Meyer, *Journal of Nanoparticle Research*, 2006, **8**, 489-496.
19. Q. A. Pankhurst, N. T. K. Thanh, S. K. Jones and J. Dobson, *J Phys D Appl Phys*, 2009, **42**.
20. S. Gangopadhyay, G. C. Hadjipanayis, B. Dale, C. M. Sorensen, K. J. Klabunde, V. Papaefthymiou and A. Kostikas, *Physical Review B*, 1992, **45**, 9778-9787.
21. O. Iglesias, A. Labarta and X. Batlle, *J Nanosci Nanotechnol*, 2008, **8**, 2761-2780.
22. F. Bodker, S. Morup and S. Linderth, *Physical Review Letters*, 1994, **72**, 282-285.
23. L. Signorini, L. Pasquini, L. Savini, R. Carboni, F. Boscherini, E. Bonetti, A. Giglia, M. Pedio, N. Mahne and S. Nannarone, *Physical Review B*, 2003, **68**.
24. K. Fauth, E. Goering, G. Schütz and L. T. Kuhn, *Journal of Applied Physics*, 2004, **96**, 399.
25. C. M. Wang, D. R. Baer, J. E. Amonette, M. H. Engelhard, J. Antony and Y. Qiang, *J Am Chem Soc*, 2009, **131**, 8824-8832.
26. J. Rockenberger, F. Nolting, J. Luning, J. Hu and A. P. Alivisatos, *J Chem Phys*, 2002, **116**, 6322-6328.
27. A. Fraile Rodríguez, F. Nolting, J. Bansmann, A. Kleibert and L. J. Heyderman, *Journal of Magnetism and Magnetic Materials*, 2007, **316**, 426-428.
28. A. Fraile Rodríguez, A. Kleibert, J. Bansmann, A. Voitekans, L. J. Heyderman and F. Nolting, *Phys Rev Lett*, 2010, **104**, 127201.
29. F. Kronast, N. Friedenberger, K. Ollefs, S. Gliga, L. Tati-Bismaths, R. Thies, A. Ney, R. Weber, C. Hassel, F. M. Romer, A. V. Trunova, C. Wirtz, R. Hertel, H. A. Durr and M. Farle, *Nano letters*, 2011, **11**, 1710-1715.
30. *Quantities, units and symbols in physical chemistry*, Blackwell Scientific Publications, Oxford, 1993.
31. A. Kleibert, J. Passig, K. H. Meiwes-Broer, M. Getzlaff and J. Bansmann, *Journal of Applied Physics*, 2007, **101**, 114318.
32. A. Kleibert, K. H. Meiwes-Broer and J. Bansmann, *Physical Review B*, 2009, **79**.
33. F. Jimenez-Villacorta, C. Prieto, Y. Huttel, N. D. Telling and G. van der Laan, *Physical Review B*, 2011, **84**.
34. V. N. Popok, I. Barke, E. E. B. Campbell and K.-H. Meiwes-Broer, *Surface Science Reports*, 2011, **66**, 347-377.

35. M. Ruano, M. Diaz, L. Martinez, E. Navarro, E. Roman, M. Garcia-Hernandez, A. Espinosa, C. Ballesteros, R. Fermento and Y. Huttel, *Physical chemistry chemical physics : PCCP*, 2013, **15**, 316-329.
36. A. Kleibert, A. Voitkans and K. H. Meiwes-Broer, *Physical Review B*, 2010, **81**.
37. L. Le Guyader, A. Kleibert, A. Fraile Rodríguez, S. El Moussaoui, A. Balan, M. Buzzi, J. Raabe and F. Nolting, *Journal of Electron Spectroscopy and Related Phenomena*, 2012, **185**, 371-380.
38. U. Flechsig, F. Nolting, A. F. Rodriguez, J. Krempasky, C. Quitmann, T. Schmidt, S. Spielmann and D. Zimoch, *Aip Conf Proc*, 2010, **1234**, 319-322.
39. A. F. Rodríguez, A. Kleibert, J. Bansmann and F. Nolting, *Journal of Physics D: Applied Physics*, 2010, **43**, 474006.
40. T. Regan, H. Ohldag, C. Stamm, F. Nolting, J. Lüning, J. Stöhr and R. White, *Physical Review B*, 2001, **64**.
41. D. J. Huang, C. F. Chang, H. T. Jeng, G. Y. Guo, H. J. Lin, W. B. Wu, H. C. Ku, A. Fujimori, Y. Takahashi and C. T. Chen, *Physical Review Letters*, 2004, **93**.
42. A. S. Khanna, *Introduction to high temperature oxidation and corrosion*, ASM International, Materials Park, OH, 2002.
43. K. Fauth, *Applied Physics Letters*, 2004, **85**, 3271-3273.
44. A. Ceylan, C. C. Baker, S. K. Hasanain and S. I. Shah, *Journal of Applied Physics*, 2006, **100**.
45. C. A. F. Vaz, E. I. Altman and V. E. Henrich, *Physical Review B*, 2010, **81**.
46. R. H. Kodama, *Journal of Magnetism and Magnetic Materials*, 1999, **200**, 359-372.
47. M. Jamet, W. Wernsdorfer, C. Thirion, V. Dupuis, P. Mélinon, A. Pérez and D. Maily, *Physical Review B*, 2004, **69**.